

REPORT DOCUMENTATION PAGE			Form Approved OMB NO. 0704-0188		
<p>The public reporting burden for this collection of information is estimated to average 1 hour per response, including the time for reviewing instructions, searching existing data sources, gathering and maintaining the data needed, and completing and reviewing the collection of information. Send comments regarding this burden estimate or any other aspect of this collection of information, including suggestions for reducing this burden, to Washington Headquarters Services, Directorate for Information Operations and Reports, 1215 Jefferson Davis Highway, Suite 1204, Arlington VA, 22202-4302. Respondents should be aware that notwithstanding any other provision of law, no person shall be subject to any penalty for failing to comply with a collection of information if it does not display a currently valid OMB control number.</p> <p>PLEASE DO NOT RETURN YOUR FORM TO THE ABOVE ADDRESS.</p>					
1. REPORT DATE (DD-MM-YYYY) 26-10-2009		2. REPORT TYPE Final Report		3. DATES COVERED (From - To) 12-May-2004 - 11-Jun-2009	
4. TITLE AND SUBTITLE Final Report			5a. CONTRACT NUMBER W911NF-04-1-0191		
			5b. GRANT NUMBER		
			5c. PROGRAM ELEMENT NUMBER 611103		
6. AUTHORS T. Russell, A. Balazs, T. Emrick, G. Tew, Q. Wang, G. Walker			5d. PROJECT NUMBER		
			5e. TASK NUMBER		
			5f. WORK UNIT NUMBER		
7. PERFORMING ORGANIZATION NAMES AND ADDRESSES University of Massachusetts - Amherst Office of Grant & Contract Admin. 408 Goodell Building Amherst, MA 01003 -3285				8. PERFORMING ORGANIZATION REPORT NUMBER	
9. SPONSORING/MONITORING AGENCY NAME(S) AND ADDRESS(ES) U.S. Army Research Office P.O. Box 12211 Research Triangle Park, NC 27709-2211				10. SPONSOR/MONITOR'S ACRONYM(S) ARO	
				11. SPONSOR/MONITOR'S REPORT NUMBER(S) 46632-CH-MUR.20	
12. DISTRIBUTION AVAILABILITY STATEMENT Approved for Public Release; Distribution Unlimited					
13. SUPPLEMENTARY NOTES The views, opinions and/or findings contained in this report are those of the author(s) and should not be construed as an official Department of the Army position, policy or decision, unless so designated by other documentation.					
14. ABSTRACT In the MURI program on Bio-Directed Hierarchical Assembly of Multifunctional Materials we have developed routes to isolate, purify and functionalize symmetric and asymmetric bionanoparticles (viruses) in large quantities; investigated their interfacial assembly; their co-assembly with synthetic block copolymers, and developed chemistries on the assembled nanoparticles for encapsulation and delivery applications. Our theoretical studies have guided us in defining the parameters that control the assemblies at fluid interfaces, in multilayered composite					
15. SUBJECT TERMS nanoparticles, self-healing, self-corralling, bionanoparticles, functionalization, Aperatureless Near Field Scanning Optical Microscopy (ANFSOM), ferromagnetic, membranes					
16. SECURITY CLASSIFICATION OF:			17. LIMITATION OF ABSTRACT UU	15. NUMBER OF PAGES	19a. NAME OF RESPONSIBLE PERSON Thomas Russell
a. REPORT UU	b. ABSTRACT UU	c. THIS PAGE UU			19b. TELEPHONE NUMBER 413-577-1516

## ***Ferritin-polymer conjugates: grafting chemistry and self-assembly***

***Grafting polyMPC and polyPEGMA from ferritin by ATRP.*** ATRP is well-known for its functional group compatibility and tolerance of aqueous conditions. We conjugated polyMPC to ferritin using grafting-from techniques, and characterized the polyMPC-grafted ferritin by NMR spectroscopy, FPLC and SDS-PAGE. These polyelectrolyte-covered particles were also characterized by TEM, and their surface charge was determined by  $\zeta$ -potential measurements. We also prepared poly(PEGMA)-grafted ferritin to compare its surface properties and self-assembly capabilities relative to the polyMPC-functionalized nanocages.

Both the polyMPC and polyPEGMA grafted ferritin samples showed the formation of very high molecular weight hybrid nanoparticles, and also reflecting the polydispersity of the grafted chains. ATRP was used to control the molecular weight of the grafted polymers, by adjusting monomer-to-initiator feed ratio. Estimating the molecular weight of the grafted polymer chains assumes complete initiation, giving an average ~45 polymer chains per particle. When the MPC-to-initiator (M:I) feed ratio was 20, the average individual polyMPC graft molecular weight was estimated to ~6.4 kDa, relatively close to the theoretical value 6.0 kDa. At M:I = 50, the estimated grafts molecular weight is 11.3 kDa. At M:I = 100, it goes to 16.4 kDa, significantly lower than the theoretical value of 29.8 kDa. And their hydrodynamic radii increased dramatically from 6.5 nm for native ferritin, to 8.9, 10.6, and 12.5 nm for polyMPC-grafted ferritin with an increased monomer-initiator ratio from 20, to 50, and 100. As with polyPEGMA-grafted ferritin, as the grafted individual polyPEGMA molecular weight increased from 3.2 kDa, to 5.7 kDa, and 13.8 kDa, their hydrodynamic radii increased from 7.7 to 8.6 and 11.6 nm, respectively, when the monomer-initiator ratio was increased correspondingly from 10, to 50, and to 100. But the higher monomer-initiator loading ratio caused a larger deviation between experimental and theoretical molecular weights of the grafted polymer, which may be due primarily to the low conversion (~50%) for the 50:1 and 100:1 cases, due to the dilute conditions required in these systems relative to typical ATRP reactions. Transmission electron microscopy (TEM) was also used to characterize the morphology and structure of the polymer-grafted nanocages. Following polymer grafting, the nanocages were found to be intact. Moreover, grafting of polyMPC and polyPEGMA led to an increase in average particle diameter.

Zeta potential measurements were performed on aqueous ferritin solutions to determine the surface charge as a function of pH. For polyMPC- and polyPEGMA-grafted ferritin, the observed zeta potential was nearly zero, and changed little with pH. The absence of a detectable surface charge in polymer-grafted ferritin indicates a highly efficient screening of the charge by the neutral polymer grafts. Interestingly, the polymer architecture and possibly grafting density was seen to strongly influence the surface charge. For ferritin grafted with low molecular weight (~750 g/mol) PEG, we found its surface charge to change significantly with pH, exhibiting only a slight screening relative to native ferritin.

***Ferritin-polymer conjugates by “grafting-to”.*** In comparative grafting-to experiments, NHS-terminated poly(PEGMA) homopolymers of various molecular weights and narrow PDI were synthesized by ATRP. A range of NHS-terminated poly(PEGMA<sub>475</sub>) structures with different molecular weights were targeted by carrying out the polymerizations at different monomer-to-NHS-initiator feed ratios, from 15 to 30. Conjugation of NHS-terminated poly(PEGMA) to ferritin was performed in PBS buffer (pH 9.0) by incubating 50-fold excess of polymer. The molecular weights of the conjugates were determined using 59, 50, and 33 polyPEGMA chains grafted to the ferritin nanocage. SDS-PAGE of the poly(PEGMA)-ferritin conjugates prepared by grafting-to reactions are seen at higher molecular weight than ferritin, and agree with the larger molecular weight grafts, consistent with FPLC result.

***Self-assembly of ferretin nanocage conjugates with PS-*b*-PEO.*** Tailoring the surfaces of protein nanocages with polymer brushes that have different affinities for the substrate should impart polymer properties to the nanocages. After polymer brushes, like polyMPC and polyPEGMA, were grafted from the ferritin nanocages, their surface affinity with PS-*b*-PEO diBCP thin films was investigated, by incubating polymer-grafted nanocages with BCP films, followed by extensive rinsing, and characterization by TEM.

An ultrathin (~26 nm) film of PS-*b*-PEO was prepared by spin-coating a 1 wt% DMF solution of PS-*b*-PEO (20 kg/mol-*b*-6.5 kg/mol) onto a clean silicon wafer with a silicon oxide layer, followed by the annealing of the film in THF for 30 minutes in a closed jar. A well-ordered phase-separated film was obtained and transferred to a carbon-coated copper grid using 5 wt% aqueous HF. Then, the film was incubated for 1 h with 500  $\mu$ L of different ferritin samples (0.5 mg/mL), including native ferritin, polyMPC-grafted ferritin, polyPEGMA-grafted ferritin. The grids were rinsed thoroughly with deionized water, dried under ambient conditions, and characterized by TEM.

Native ferritin was found to preferentially segregate to the PS microdomains, since PS is more hydrophobic than PEO. This is in keeping with earlier studies where it has been shown that hydrophobic surfaces can adsorb more proteins than hydrophilic surfaces. Interestingly, polyMPC and polyPEGMA-grafted ferritin, with their hydrophilic surface coverage, did not show substantial uptake into the hydrophilic PEO domains, but rather showed a suppressed adsorption on the film. The lack of adsorption of polymer-grafted ferritin in these cases reflects the inherent ‘anti-fouling’ properties of this surface coverage.

***Polymer-grafted nanocages in diBCP thin films by co-assembly.*** Poly(PEGMA)-grafted ferritin was soluble in chloroform, benzene and DMF. HPLC confirmed the stability of poly(PEGMA)-coated ferritin, giving an same elution volume as fresh sample in water even upon storage in DMF for at least one day. The ability to process ferritin in DMF provides the opportunity to study its assembly behavior with BCPs such as PS-*b*-PEO. TEM confirmed the oriented cylindrical microdomain morphology and also showed the location of the particles in the PEO cylinders. The average center-to-center distances between BCP microdomains was

determined by GISAXS. For the polymer film loaded with low molecular weight PEG<sub>750</sub>-modified ferritin particles, the center-to-center distance was 43.1 nm, which is larger than 37.6 nm of PS-*b*-PEO film. The PEG<sub>750</sub>-ferritin nanoparticles can increase the size of PEO microdomains and, due a difference in the cross-sectional area of chains at the interfaces, can cause a reduction in the size of the PS domains. The overall result of incorporating the PEG-ferritin nanoparticles in the PEO microdomains is to increase the PEO microdomain size and increase the center-to-center distance between the PEO microdomains. PolyPEGMA-grafted ferritin nanoparticles are ~15.6 nm in diameter and, when loaded into the PS-*b*-PEO GISAXS results indicate in an increase of the center-to-center distance between PEO microdomains to 47.3 nm.

### ***Guided Assemblies of Bionanoparticles***

***Preparation of pre-patterned gold dots in the silica substrate by block copolymer micelle lithography.*** Amphiphilic block copolymers of polystyrene-*block*-poly(4-vinylpyridine) (PS-*b*-P4VP) self-assemble into micelles in toluene/ THF (7/3, v/v) which is a selective solvent for PS. The PS blocks form a shell around the less soluble P4VP blocks to minimize nonfavorable interactions with the solvent. The micellar core-shell structure forms a nanoreactor that allows for the selective dissolution of metal precursor salts into the P4VP core or the synthesis of monodisperse metal nanoparticles in each core .

Spin coating a PS-*b*-P4VP solution from a toluene/ THF mixture onto a cleaned silica wafer produces a randomly packed array of micelles, as shown in the scanning force micrograph in Figure 1.. By exposing this randomly packed array to THF vapors for 4 hrs. allows the lateral packing of the micelles to improve, as shown in the SFM imgs in Figure 1b. After removing all the THF, the planar micellar array was immerse in a 1 wt% ethanol solution of HAuCl<sub>4</sub> to allow the gold precursor to complex with P4VP. Then the gold precursor was then reduced to gold nanoparticles using an oxygen plasma which also removes the copolymer entirely, as shown by detailed XPS investigations. SEM image of the gold arrays show the particle size is 21.9±1.8 nm in diameter with a narrow Gaussian size distribution. The size of the golds nanodots is controlled by the amount of metal precursor added to P4VP microdomains. The gold nanodots are much smaller than size of the P4VP microdomains which is expected

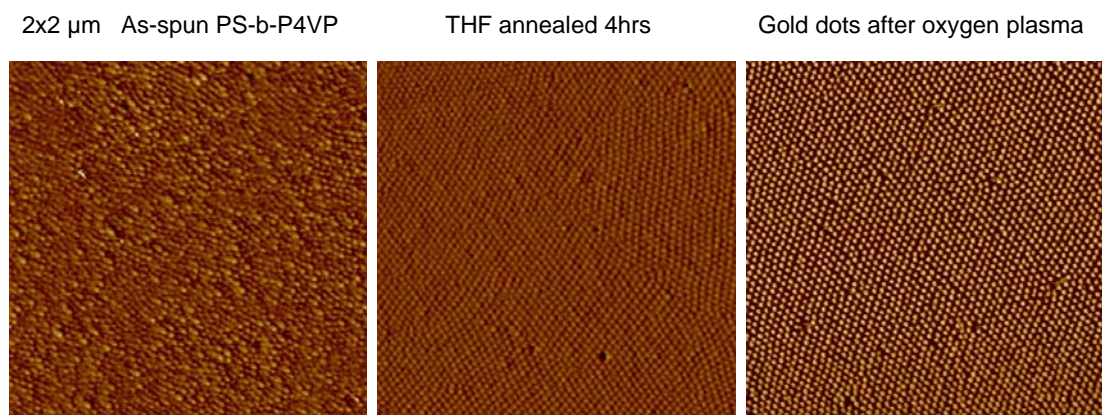
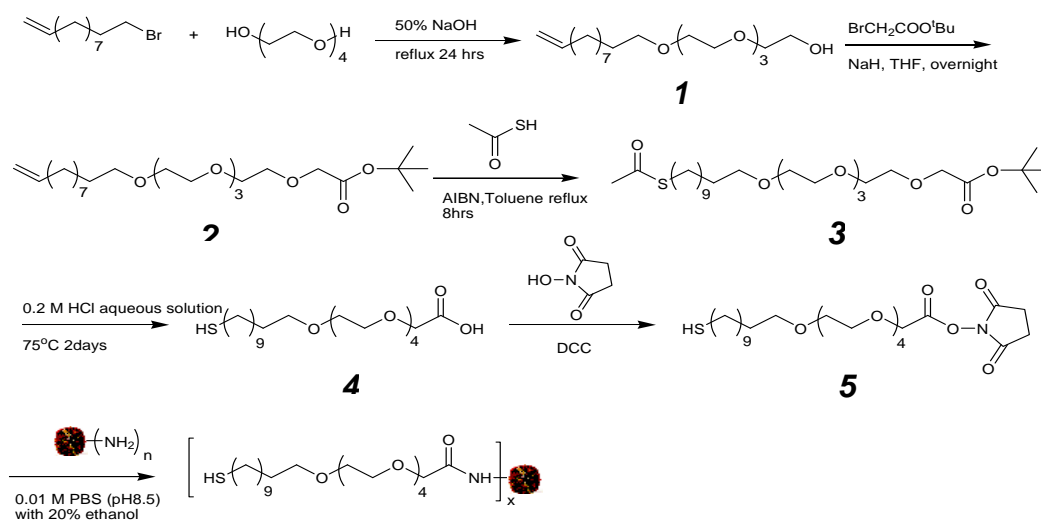


Figure 1 Scanning force microscopy phase images

**Synthesis of thiol-modified ferritin nanoparticles.** Small molecules having thiol functionality were attached to the ferritin surface to promote the anchoring of the ferritin to the gold posts. So 11-mercaptoundecyl-tetra-(ethylene glycol) NHS ester was designed and synthesized by integration of tetraethylene glycol into the alkylated thiol ligand to resist the nonspecific protein adsorption on the substrate, and then this compound was coupled with ferritin through NHS ester and amine chemistry to introduce the thiol functionality.

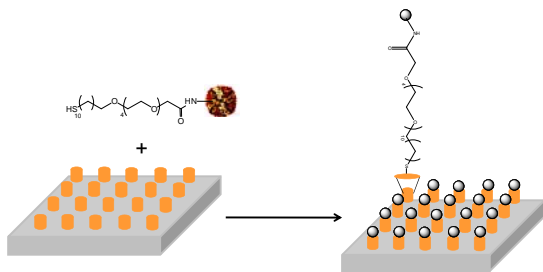
FPLC traces of Superose 6 10/300 size exclusion column confirmed that modified ferritin nanoparticles were intact and had a similar elution volume at 13.152 mL as the original ferritin when using PBS buffer as eluent. MALDI-TOF profile of the purified product, indicated that MW of thiol-modified ferritin shifted to a high molecular weight by 769 dalton from 20,131 (MW of ferritin subunit) to 20,900 (MW of modified ferritin subunit),



Scheme 1 Synthesis of thiol-modified ferritin nanoparticles

corresponding to 1.7 thiol moieties attached to every subunit of ferritin and 41 thiol moieties on each modified ferritin bionanoparticle. After functionalization the decrease of positive charge groups on ferritin. TEM confirmed the retention of the spherical shape of thiol-modified ferritin bionanoparticles with a diameter of 12 nm. The thiol-modified ferritin was also labeled with fluorescein isothiocyanate (FITC). The resultant ferritin nanoparticles have excitation and emission wavelengths of ~490 nm/518 nm, which are similar to FITC molecule.

***Self-assembly of thiol-modified ferritin nanoparticles in patterned gold dots template.*** After incubating thiol-modified ferritin nanoparticles in the presence of the gold-nanodot template, as shown in Scheme 2, followed a thorough rinse to remove excess ferritin, the thiol-modified ferritin nanoparticles were seen to assemble on the gold nanodots, due to the strong binding between the thiol groups and the gold. XPS measurements on the substrate surface showed that atomic percentage of gold on the surface decreased and of nitrogen increased as ferritin was anchored to the surface. The fluorescence microscopy showed that the fluorescence intensity is strong over the entire substrate that is patterned, confirming the presence of the ferritin. SEM shown in Fig.8 demonstrates attests to the fidelity in the anchoring of the ferritin to the gold nanodots where a highly ordered array is observed having features  $11.2 \text{ nm} \pm 0.7 \text{ nm}$  in diameter, consistent with the size of ferritin. The size-histogram and distribution curves of the nanoparticles in Fig.9 shows that the ferritin, anchored to the gold nanoposts, is much narrower distribution than that of the gold nanodots, as would be expected. It should be noted that the original gold nanoposts have a diameter larger than that of the ferritin. Even still, only the ferritin is effectively observed which may arise for the curvature of the tip, the curvatures of the ferritin, and the diameter of the ferritin, resulting in a shadowing of the gold nanoposts by the ferritin. Ferritin, of course, is charged and the charge can be controlled by the pH of the incubation medium. This negative charge on the ferritin establishes a repulsive interaction between the ferritin and, also, with the substrate, which has a latent negative charge. These nonfavorable interactions maintain the displacement of the ferritin at a given distance from the substrate and enhance the lateral ordering of the ferritin. Key to this is that the ferritin is not rigidly attached to the substrate but, rather, tethered to the substrate with a flexible linker.



Scheme 2. chematic of anchoring ferritin to gold nanodots.



The lateral ordering of the ferritin can, also be seen by scanning force microscopy. Shown in Figure 2 is a  $3 \times 3 \mu\text{m}^2$  area where ferritin has been anchored to gold nanoposts. Over this entire area, the anchoring of the ferritin and the lateral ordering of the ferritin is essentially perfect with no defects. Each gold nanopost has only one ferritin anchored to it and every nanopost has a ferritin attached

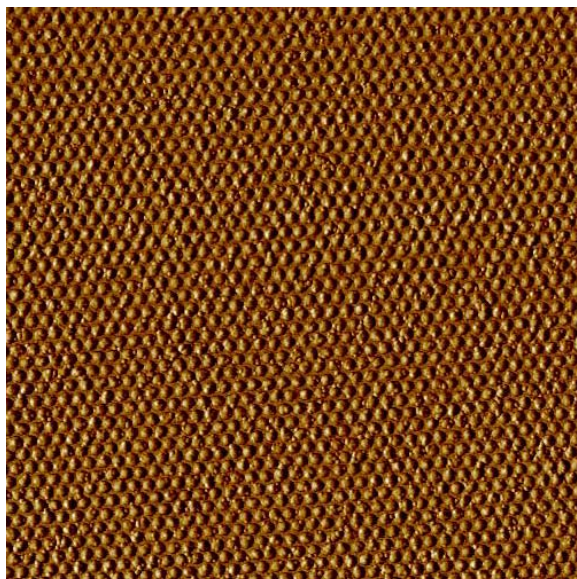


Figure .2. SFM phase image of ferritin arrays in the Hitachi-made gold pattern ( $3 \times 3 \mu\text{m}$ )

### ***Chemoselective modification of M13 bacteriophage and cell imaging***

We systematically investigated the chemical modification of three kinds of reactive groups, i.e. amino groups of lysine residue or *N*-terminal, carboxylic groups of aspartic acid or glutamic acid residues, and phenol groups of tyrosine residues, on M13 surface. The reactivity for each group was identified by conjugation with small fluorescent molecules. Furthermore, the regioselectivity of each reaction was carefully investigated by HPLC-MS-MS. By optimizing the reaction condition, a highly fluorescent M13 bacteriophage could be prepared with tailoring with hundreds of fluorescent moieties per phage particle. Additionally, cancer cell targeting motifs such as folic acid could also be conjugated onto the M13 surface. Therefore, dual-modified M13 particles by folic acid and fluorescence dye molecules were synthesized via the selective modification of two kinds of reactive groups. Such dual-modified M13 particles showed very good binding affinity to human KB cancer cells, which demonstrated the potential applications of M13 bacteriophage in bioimaging and drug delivery.

For example, combining amine and tyrosine bioconjugation, the dual-modified M13 bacteriophage could be readily prepared. M13 was first treated with fluorescein *N*-hydroxysuccinimidyl (NHS) ester to get a 190 fluorescein units tailored bacteriophage. After purification, the dye modified M13 could be further modified with azide-folate by a two-step tyrosine reaction. As shown in Figure 3, 5596 *m/z* peak indicates the fluorescent dye modification, and the peak at 5890

indicates around 400 folic acid molecules are successfully conjugated onto the M13 surface. The modified M13 bacteriophages were stable and remained intact confirmed by TEM.

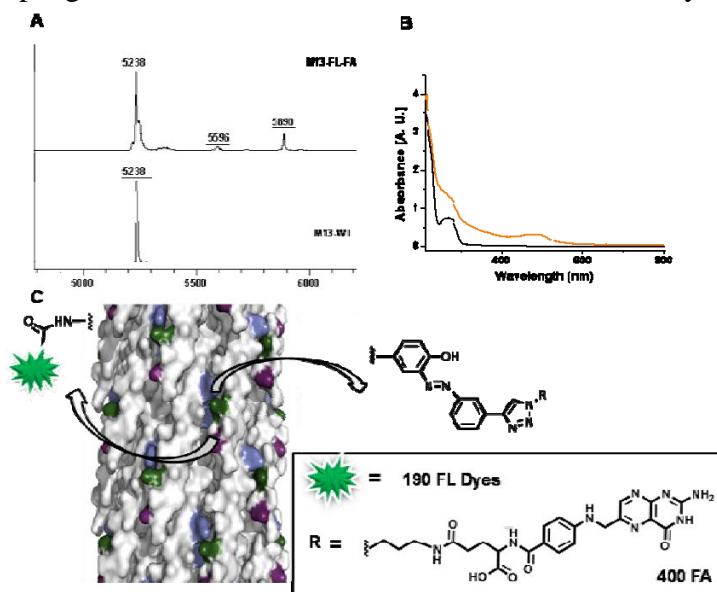


Figure 3. (A) MALDI-TOF MS of whole subunit of WT-M13 and M13 after dual modification with fluorescein *N*-hydroxysuccinimidyl (NHS) ester and folic acid. WT peak = 5,238 m/z, the dual modification shows the peaks of 5,596 m/z and 5,890 m/z indicating the fluorescein and folic acid conjugation. (B) UV-vis spectra show bacteriophage absorbance of WT-M13 (black line) and dual modified M13 bacteriophage (orange line) after purification. (C) The surface structure of M13 bacteriophage with highlights of amines and tyrosines conjugation.

The dual modified M13 bacteriophage was investigated for its potential application in tumor cell targeting. HeLa contaminant KB cells were used for the targeting study. Before imaging study, the KB cells were cultured in the folate free mediate to promote the overexpression of the folate binding proteins. The cellular uptake (Figure 4) of M13 bacteriophages in KB cells were analyzed by fluorescence microscopy. After 1 hour, 8 hours and 24 hours incubation of different samples with KB cells, the cells were fixed and taken images. The dual modified M13 bacteriophage (FA-M13-FL) shows higher cell uptake than the M13 bacteriophage which was only modified with fluorescein (M13-FL). Furthermore, FA-M13-FL particles can more efficiently label KB cells than small molecule probe - fluorescein-folate conjugate (FA-FL). The cell uptake of dual modified M13 bacteriophage showed significant increasing by long time incubation.



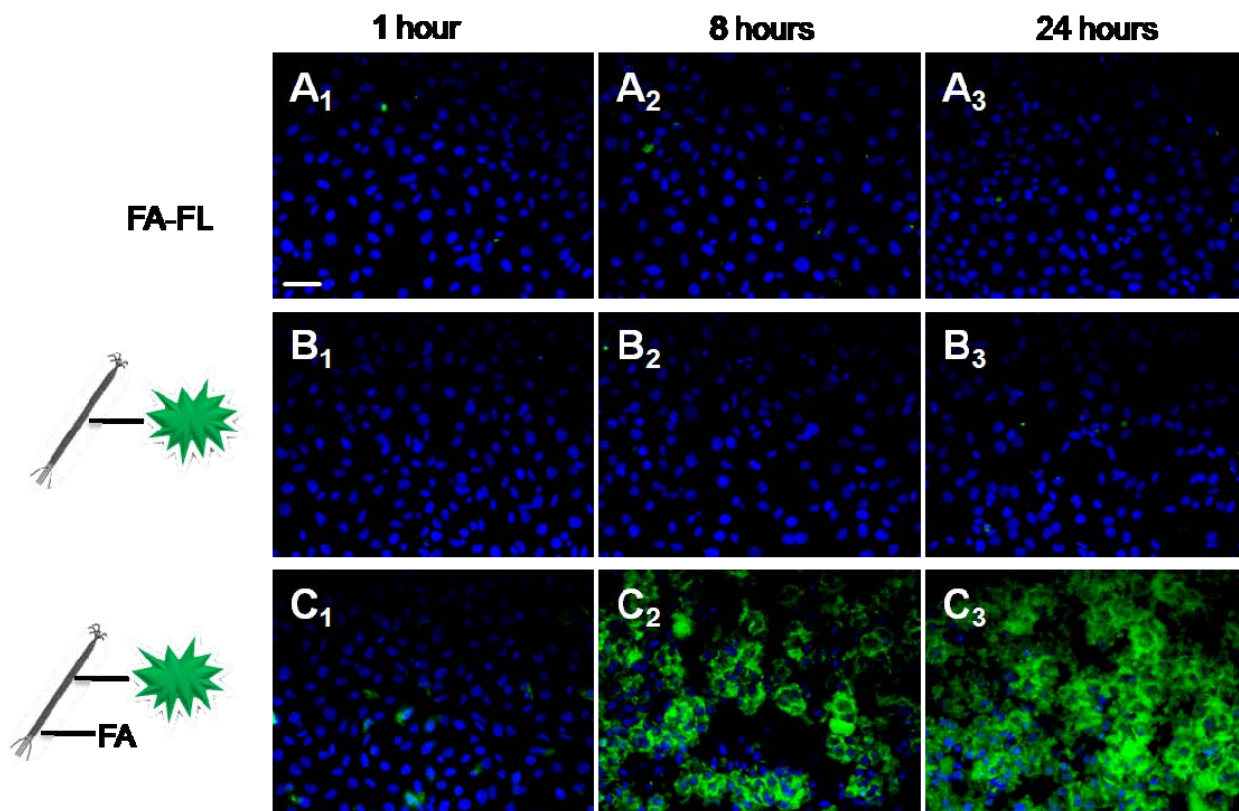


Figure 4. (A<sub>1</sub>-A<sub>3</sub>) Binding and internalization images of FA-FL into KB cells. (B<sub>1</sub>-B<sub>3</sub>) Binding and internalization images of M13-FL into KB cells. (C<sub>1</sub>-C<sub>3</sub>) Binding and internalization images of dual modified M13 bacteriophage into KB cells. The incubation times were 1 h (column 1), 8 h (column 2), and 24 h (column 3), respectively. Scale bar is 50  $\mu$ m for all images.

### *Development of polymer-bionanoparticles core-shell structures via co-assembly*

Bionanoparticles (BNPs) based core-shell structures provide a unique system for the investigation of biological interactions such as protein-protein and protein-carbohydrate interactions. However, it is still a challenge to prepare the BNPs-based core-shell structures. We recently developed two approaches to synthesize such particles: (i) co-assembly method and (ii) template synthesis method in the development of polymer-BNPs core-shell structures. These two methods can be divided into three different systems A, B, and C. In system A, different polymers including poly(2-vinylpyridine) (P2VP), poly(4-vinylpyridine) (P4VP) and poly ( $\epsilon$ -caprolactone)-*block*-poly(2-vinylpyridine) (PCL-*b*-P2VP) can form a raspberry-like structure with BNPs (Figure 5).

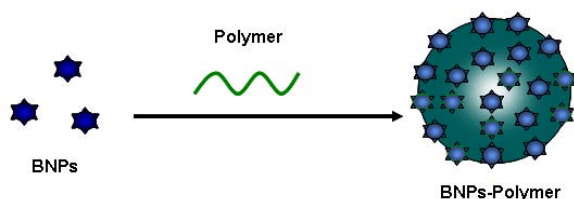


Figure 5. Schematic of BNPs-polymer core-shell structures by co-assembly.

A numbers of BNPs including cowpea mosaic virus, turnip yellow mosaic virus, and bacteriophage P22, can form such core-shell structures by the self-assembly approach. For example, bacteriophage P22, with a diameter of around 60 nm, is assembled from 420 copies of protein subunit with the aid of approximately 300 copies of the scaffolding proteins (Figure 6). The diameter of P22 particles is around 60 nm, as clearly observed in Figure 6b. P22 particles are readily obtained in large quantities; around 100 mg can be purified from one liter of culture. In addition, P22-based materials can be potential used as the molecular devices. In our study, similar core-shell P22-P4VP assemblies could be also prepared using the co-assembly method and characterized by TEM (Figure 6c) and SEM (Figure 6d).

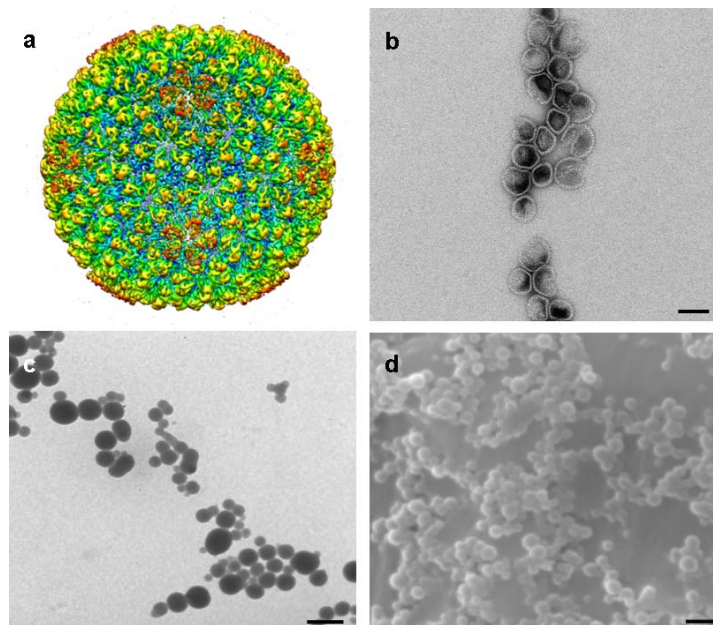


Figure 6 (a) Cryo-EM reconstruction of the structure of P22. (b) TEM image of P22 particles. (c) and (d) Representative TEM and SEM images of P22-P4VP assemblies, respectively. Scale bars: 50 nm for (b) and 500 nm for (c) and (d), respectively.

Moreover, we found that P4VP with different molecular weight could also form core-shell structures via co-assembly with BNPs. Figures 7a-b shows the transmission electron microscope (TEM) and field emission scanning electron microscopy (FESEM) images of CPMV-P4VP<sup>160</sup> using high molecular weight P4VP (160K Da) as starting materials. As shown in Figure 5a, after assembly, spherical composite particles with diameters ~ 200 nm were readily prepared. Inset 7a shows the enlarged TEM image of one single CPMV-P4VP assembly, where the rough edge can be clearly observed. A high-resolution FESEM (Figure 7b) image clearly shows that CPMV particles are covered on the surface of P4VP, similar to the core-shell product with low molecular P4VP as polymer component. The same strategy can also be used to prepare other polymers such as CPMV-P2VP and CPMV-PCL-*b*-P2VP core-shell structures. As shown in Figure 7c and 7d, after co-assembling with P2VP and PCL-*b*-P2VP, spherical core-shell assemblies CPMV-P2VP and CPMV-PCL-*b*-P2VP were readily prepared. More interestingly, biodegradable copolymer PCL-*b*-P2VP and its analogs may have potential to be used in the design and fabrication of drug delivery vehicles.

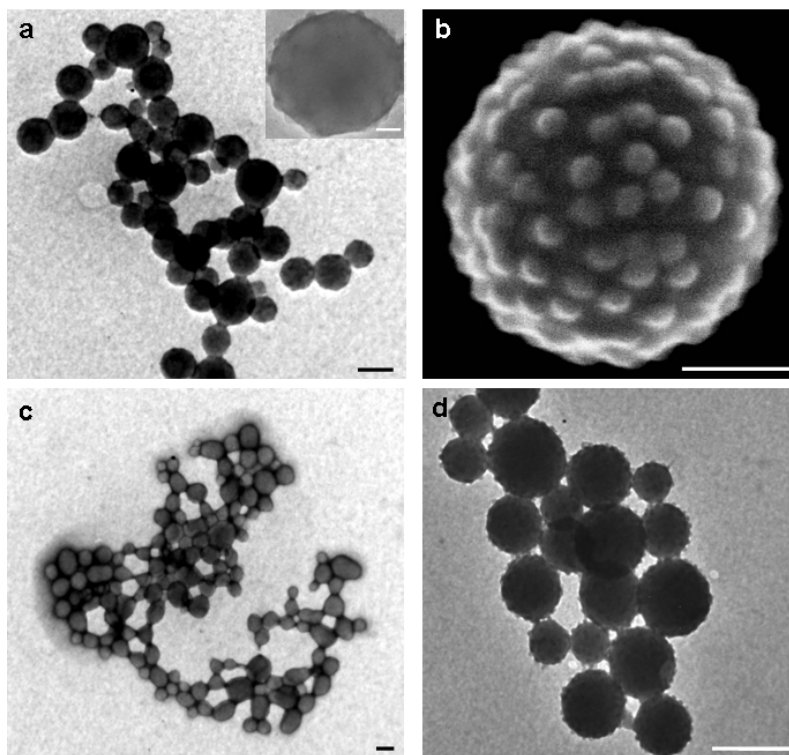


Figure 7. (a) TEM image of CPMV-P4VP<sup>160K</sup> assembly. The inset is an enlarged image of a single particle. (b) FESEM image of CPMV-P4VP<sup>160K</sup> assembly. (c) and (d) are TEM images of CPMV-P2VP and CPMV-PCL-*b*-P2VP samples, respectively. Scale bars: 400 nm for (a, c, d), 100 nm for (b), and 50 nm for the inset image of (a), respectively.

### *Development of polymer-BNPs core-shell structures via templated synthesis*

In another approach, polystyrene (PS) spheres end capped with free amine and BNPs can form a core-shell structure (Figure 8). In addition, layer-by-layer (LBL) method can also be used to prepare positive charged PS particles, which can be used as a template to form the core-shell structures with BNPs. These two methods may open a new way for preparing novel protein-based functional materials for potential applications in the biomedical field.

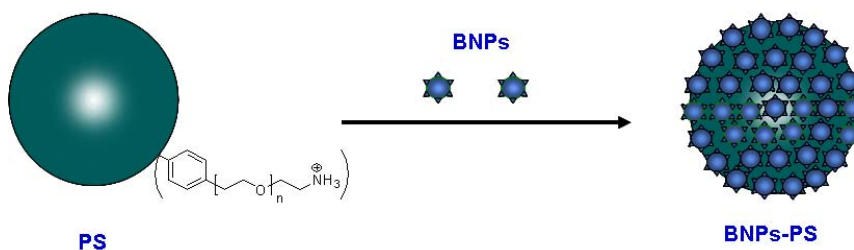


Figure 8. Schematic illustration of the formation of BNPs-PS core-shell structures by template synthesis. PS spheres end capped with free amine groups are used as the template.

In a typical procedure, CPMV coated PS structure was prepared by just simply mixing PS beads ( $\sim 130\ \mu\text{m}$ ) with CPMVs in buffers. To better visualize the formation of the core-shell structure, CPMV was first labeled covalently with the NHS-Rh dye to form CPMV-Rh following the literature method.<sup>19</sup> UV-Vis and fast protein liquid chromatography (FPLC) showed that the rhodamine was conjugated to the surface of CPMV and the CPMV particles were still intact after the modification (data not shown). Figure 9a-c shows the SEM images of the CPMV-Rh-PS particles with average diameters of  $10\ \mu\text{m}$ ,  $130\ \mu\text{m}$ , and  $320\ \mu\text{m}$ , respectively. It can be clearly observed that all the particles have the uniform diameters. Also, fluorescence microscope was used to characterize the CPMV-Rh-PS particles. After coating CPMV-Rh onto polystyrene beads surface, composite particles showed strong red colors under fluorescence microscopy, indicating the rhodamine labeled CPMV particles were coated on the PS beads (Figure 9d-f). In order to confirm that the fluorescent signals were from the CPMV-Rh not PS, a control experiment was performed by checking the fluorescence microscope image of PS beads. The results showed that there were no fluorescence signals for the PS particles (data not shown). Another concern is whether CPMVs are only located on the surface of CPMV-PS, which can be answered from the cross section analysis of confocal microscopy. The fluorescent ring shown in the inset of Figure 9e indicates that viral particles were only coated on the surface of PS beads.

Once the location of CPMV on the PS beads was investigated, the surface morphology of CPMV-PS structures was evaluated by FESEM. Figure 10a shows the typical SEM images of CPMV-PS particles ( $\sim 130\ \mu\text{m}$ ) with a narrow size distribution. As the magnification of FESEM increased, it was observed that CPMV particles formed long-range ordered structures on the surface of PS beads, as shown in Figure 10d. Similar methods can be used to assemble different BNPs such as spherical P22 and rod-like TMV. Based on the SEM and FESEM results, P22 (Figure 10b, e) and TMV (Figure 10c, f) all formed the long-range ordered structures on the PS surface. Especially for TMVs, they formed the liquid crystalline like structures on the PS beads.

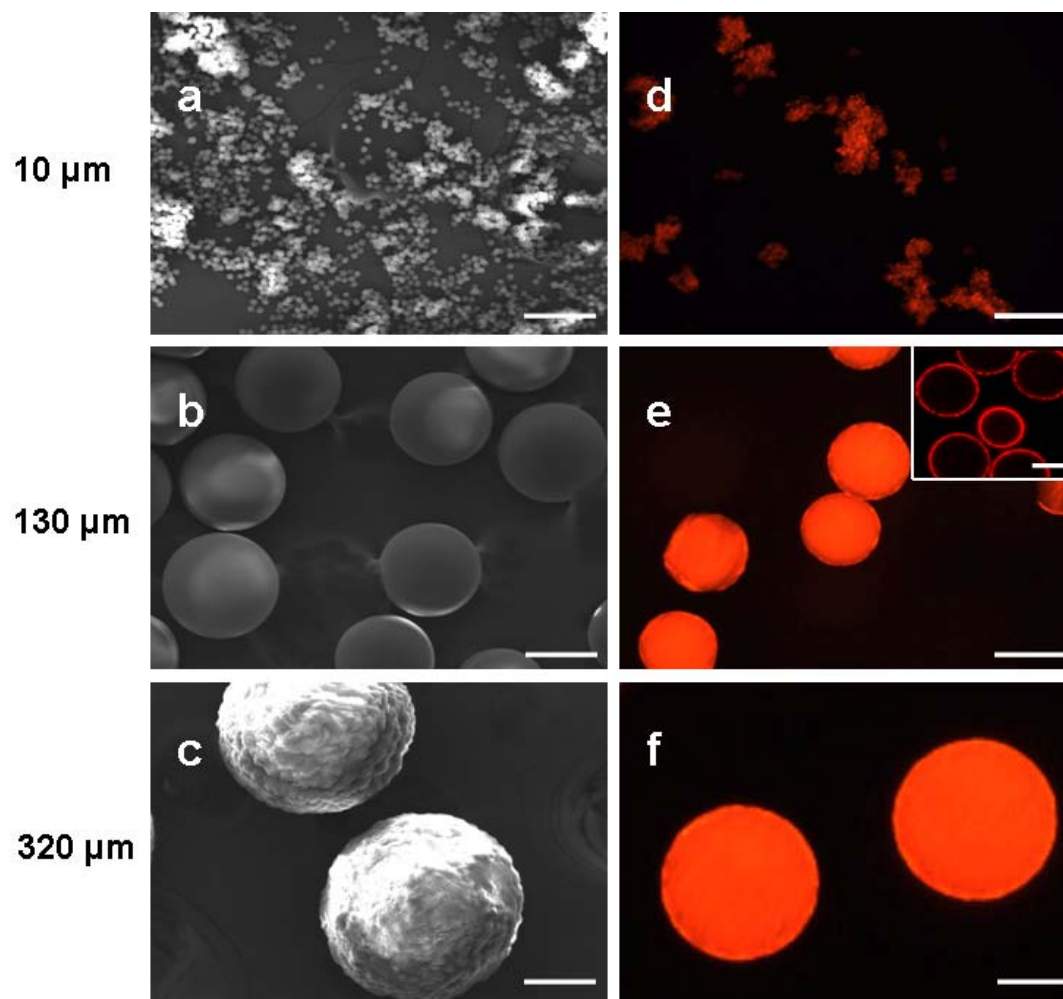


Figure 9. Scanning electron microscopy (a-c) and fluorescent microscopy image (d-f) of CPMV-Rh-PS particles with average diameters of 10  $\mu\text{m}$ , 130  $\mu\text{m}$ , 320  $\mu\text{m}$ , respectively. Inset of (e) is the cross-section confocal fluorescence image of CPMV-Rh-PS assemblies. The fluorescent signals in d-f are from the Rh modified CPMV particles. Scale bars are 100  $\mu\text{m}$ .



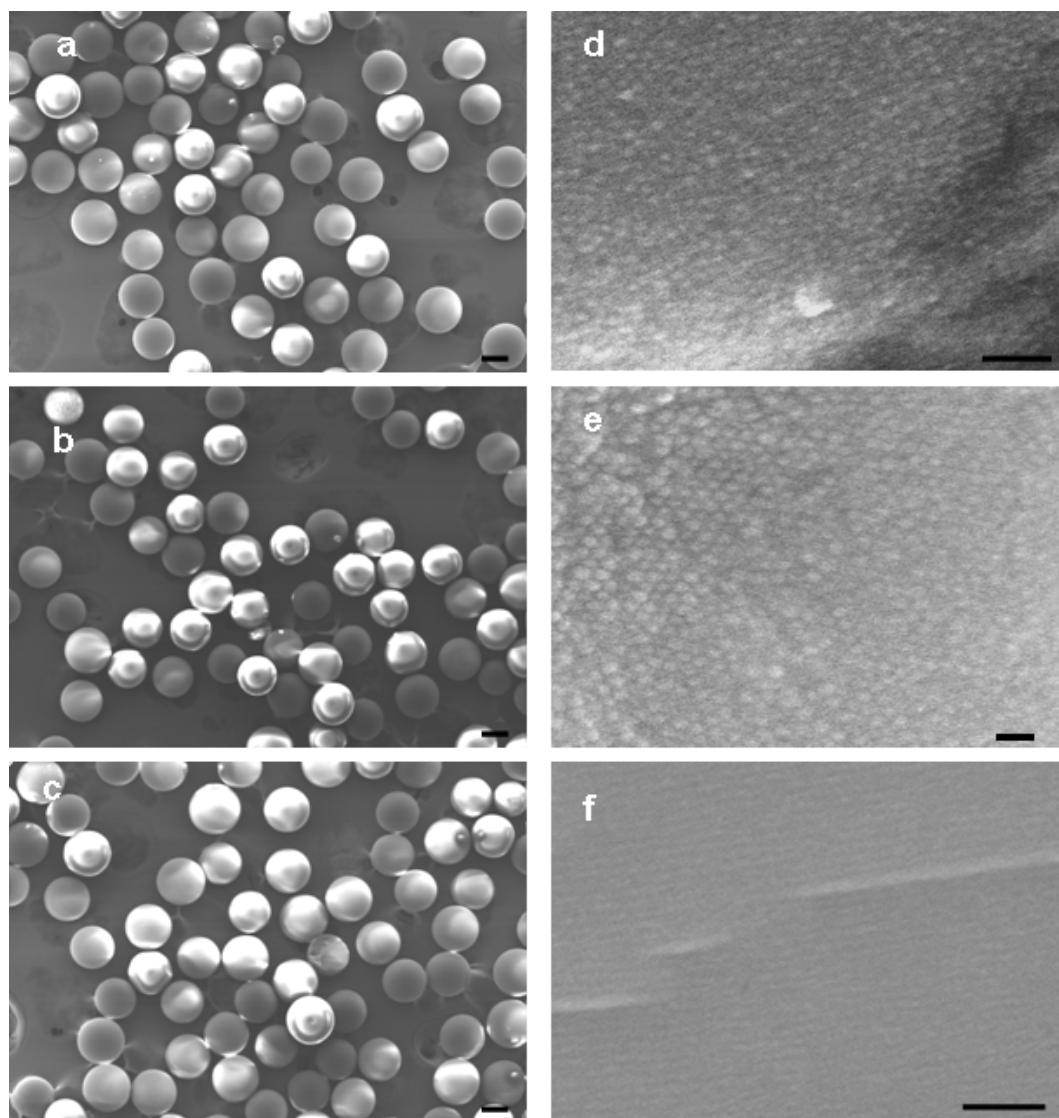


Figure 10. Low magnification of SEM image (a-c) and high magnification FESEM image (d-f) of CPMV-PS, P22-PS, and TMV-PS particles, respectively. The PS beads of 130  $\mu\text{m}$  diameter were used in the study. Scale bars in a-c and d-f are 100  $\mu\text{m}$  and 100 nm, respectively.

**Development of polymer-protein core-shell structures.** We found that proteins could also form core-shell structures through co-assembling with P4VP and other biodegradable copolymers such as poly( $\epsilon$ -caprolactone)-block-poly(2-vinyl pyridine) (PCL-b-P2VP). Compared to the template synthesis method, our system has its unique advantages: (i) the structures can be easily formed based on the co-assembly of polymers and proteins; (ii) size-controlled nanoparticle-proteins structures can be readily obtained by changing the mass ratios of polymers and proteins; (iii) proteins still retain their functionalities especially for some antibodies such as apolipoprotein, which can be used as the potential drug delivery vehicles. The formation of such core-shell structures are mainly based on the electrostatic interactions between P4VP and proteins. In order to confirm it, the co-assembly behaviors between proteins and P4VP were studied at various pH conditions. The assembly behaviors between proteins and P4VP were conducted at different pH



of 5.5, 6.5, 7.8, 9.4, and 11.7, respectively. The proteins chosen were Pep (pI 2.8), TMV (pI 3.5), BSA (pI 4.8), Lip (pI 5.6), HRP (pI 7.2), ChT (pI 8.7), Pap (pI 9.6), and Rib A (pI 9.4). Figure 10 shows the phase diagram of proteins-P4VP at different pH values. The results further confirmed our hypothesis that the electrostatic interactions are a major driving force for the formation of core-shell structures. Therefore, based on this diagram, a variety of core-shell structures can be easily prepared using different proteins under different buffer conditions.

**Development of new fluorescent crosslinkers.** Cu(I) catalyzed alkyne-azide cycloaddition (CuAAC) reaction, a typical Click reaction, is one of the modular synthetic approaches which has been broadly used in various organic synthesis, medicinal chemistry, materials development and bioconjugation applications. For the first time, we have developed two dialkyne derivatized fluorescent crosslinkers which can be applied to crosslink two biomolecules using CuAAC reaction (Figure 11).

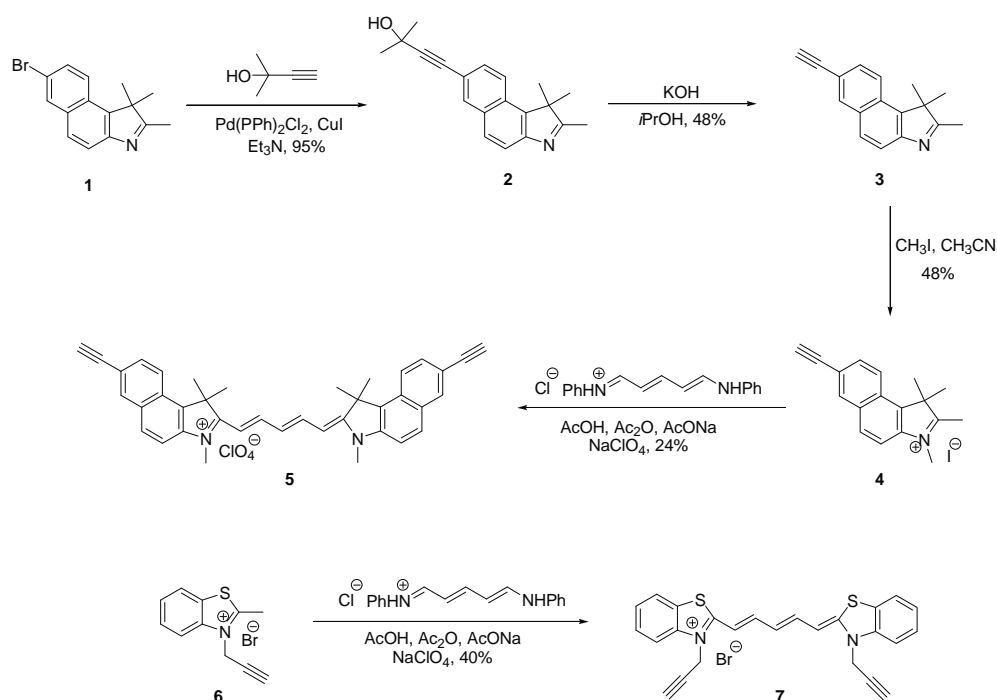


Figure 11. Synthetic route for fluorescent crosslinkers.

Turnip yellow mosaic virus (TYMV), a plant virus with unique structural and chemical properties, was used as prototypical scaffold in this study. TYMV can be efficiently crosslinked with reported linkers using CuAAC reaction. Upon crosslinking, the fluorescence of both linkers diminished, likely due to the distortion of the polymethylene backbone, which therefore can be used to indicate the completion of the reaction.

### **Assembly of TYMV on a planar oil/water interface**

To achieve highly ordered 2-D assemblies of TYMV, other factors that govern the self-assembly process at planar O/W interface such as ionic strength of the aqueous phase, pH of the buffer

solution, concentration of amine DHAA and nature of the organic or oil phase were optimized. The assembly process was carried out in a closed chamber and equilibrated for 2 hr. TYMV was cross-linked using glutaraldehyde. The cross-linked layer of TYMV was transferred to the surface of the wafers and grids for microscopy experiments. The formation of highly ordered 2-D hexagonal arrays of TYMV nanoparticles is evident in the TEM and SFM micrographs as shown in Figure 12. *In-situ* X-ray scattering confirmed the ordering of the TYMV at the interface but the electron density contrast was too small to quantitatively assess the thickness of the layer. Shown in Figure 12d is a Voronoi diagram where the hexagonal packing of the TYMV dominated the packing with very small neighbor packing defects in the assembly. The distribution of the normalized center-to-center distances  $a/\langle a \rangle$  in the TEM image (Figure 12c) is shown in Figure 12e. A narrow distribution was seen which is consistent with the high degree of ordering. The orientational correlation function of the particle center locations in the TEM image (Figure 12c) was calculated in Figure 12f. The profile shows very little decay even at very large distances  $r = 30a$ , which supports the long-range ordering of the TYMV.

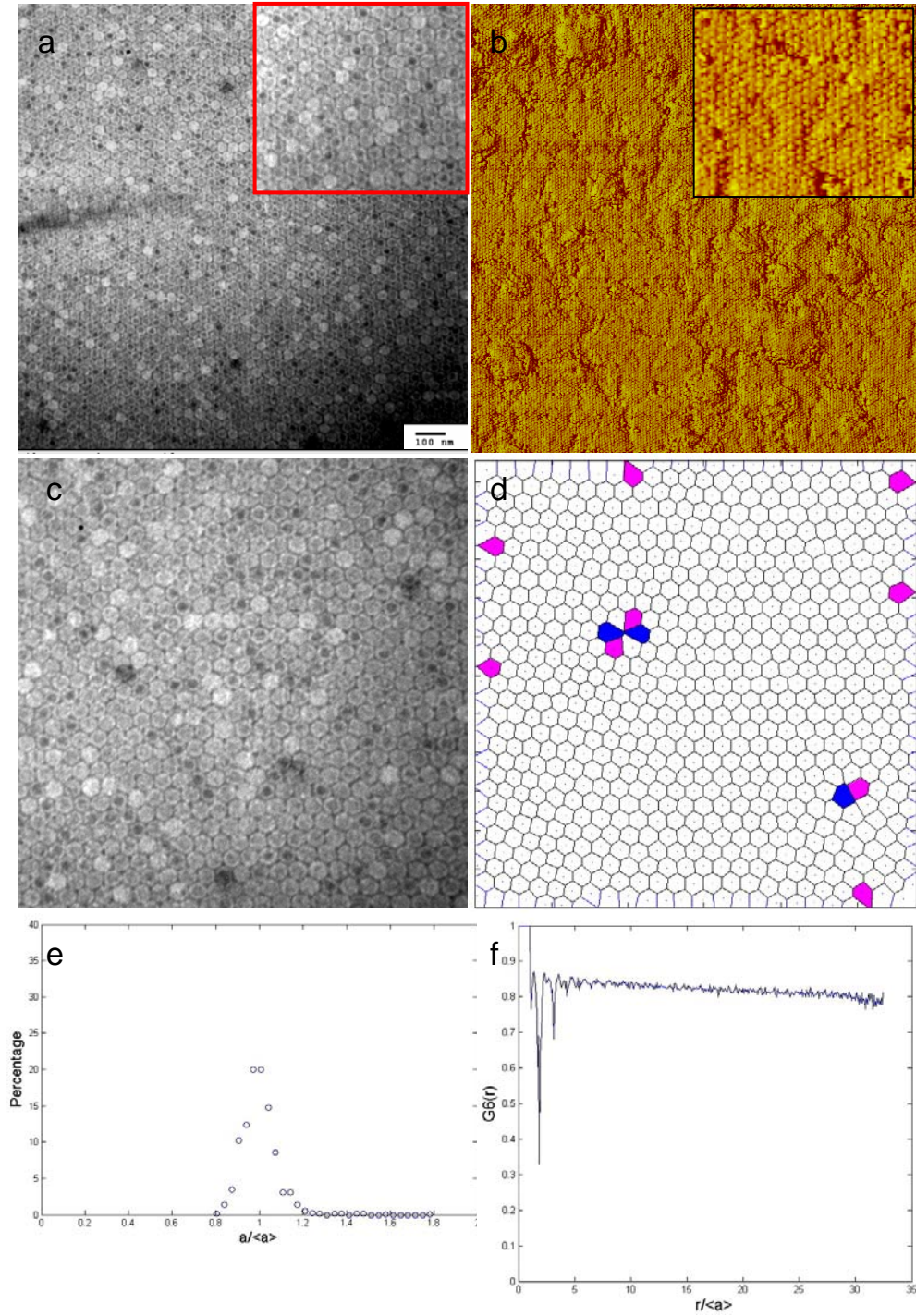
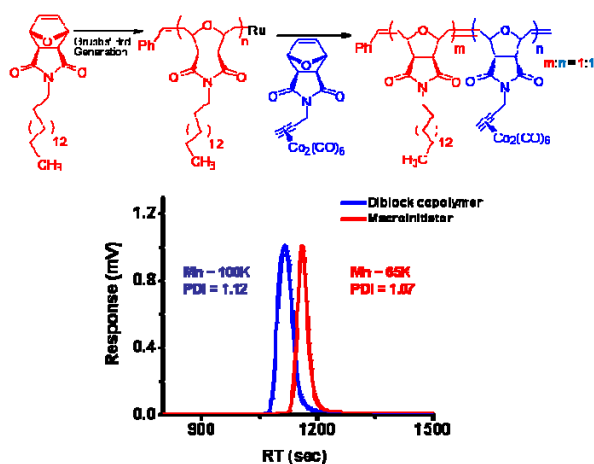


Figure 12. (a) TEM image of hexagonally assembled TYMV particles at the O/W flat interface, the layer was transferred to the TEM grid from the interface directly. (b) SFM phase micrographs of interfacial layer, of the self-TYMV nanoparticle monolayer transferred directly onto a glass surface from the O/W interface. (c) TEM image used for image analysis. (d) Voronoi diagram constructed from the particle center locations in image a. TYMV nanoparticles having four, five, six and seven nearest neighbors are marked in blue, pink, white and green, respectively. (e) Distribution of the normalized particle center-to-center distances  $a/\langle a \rangle$  in the Voronoi diagram shown in (d), where  $\langle a \rangle$  is the average particle center-to-center distance. (f) Orientational order correlation function calculated from c.

## Confinement Induced Magnetic Materials

Coupling self-assembly to the generation of magnetic materials in a facile, straight forward manner has remained a challenge. We have designed novel block copolymers (BCP) that are pre-programmed with the necessary chemical information to microphase separate and deliver room temperature ferromagnetic properties upon a simple heat treatment. The importance of the nanoscopic elements is demonstrated by comparison with the parent homopolymer which yields only paramagnetic materials even though chemically identical and with a higher loading of the magnetic precursor. In addition to the room temperature ferromagnetic properties generated from the block copolymer, the *in situ* generation densely functionalizes the surface of the nanoscopic elements which renders them oxidatively stable.

Below is the chemical synthesis and structure of the block copolymers. Using ROMP, we have successfully synthesized a host of various block lengths.



As can be seen in Figure 13, the block copolymer is a room temperature ferromagnetic while the homopolymer is only paramagnetic. Not shown are the TEM and SAXS data which confirm that the block copolymer is nanostructured while the homopolymer is simply an amorphous material.

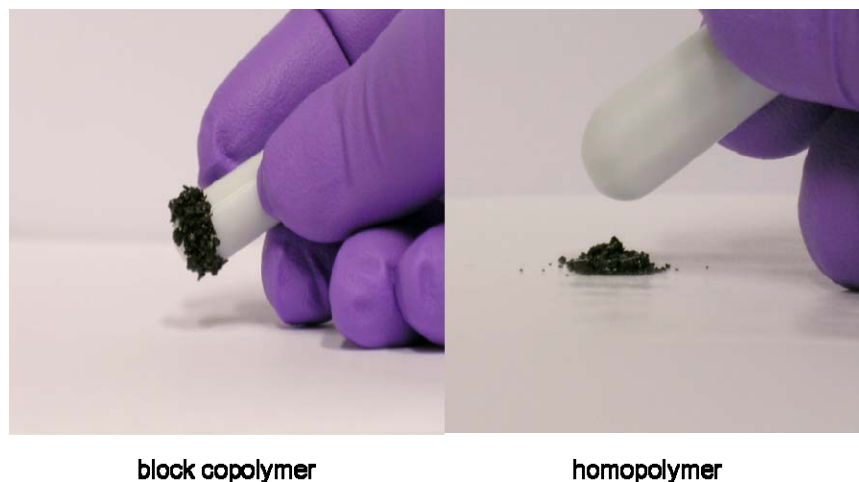


Figure 13. Demonstration of magnetic properties of copolymer (lhs) to those of a homopolymer (rhs).

Interestingly, while the block copolymer is magnetic at room temperature, to date, all evidence indicates that the cobalt particles within the material are amorphous. This is documented below in a series of WAXD studies. Initially, we are concerned that the cobalt particles were too small for WAXD so we synthesized Cobalt nanoparticles in solution. This results in crystalline particles roughly 10 nm in diameter. When these particles were mixed with the homopolymer and studied, a broad peak for crystalline Cobalt was observed. In contrast, neither polymer showed cobalt-like diffraction peaks when annealed at 200 °C but both showed them when pyrolyzed at 600 °C.

### ***Protein Channels***

We present results from our investigations on the interactions between different models for synthetic protein channels, and the bi-layer membrane of a vesicle. Since the channels will typically interact with a small patch of the vesicle membrane whose radius of curvature is much larger than the vesicle radius, we consider a representative bi-layer membrane patch interacting with the protein channel. The bi-layer is composed of two

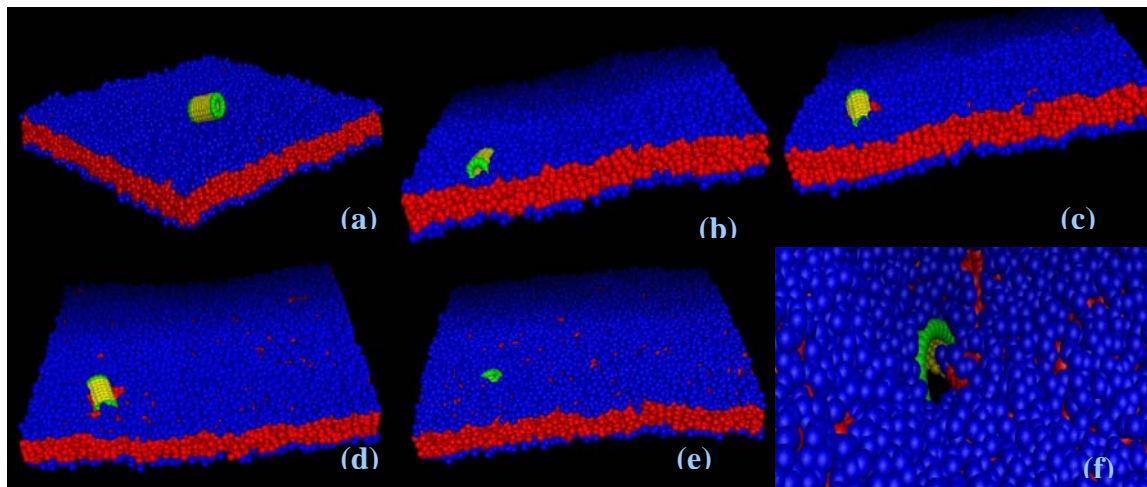


Figure 14. Insertion of a channel of radius  $1 r_c$  ( $\sim 0.67$  nm) and length  $5 r_c$  into a bi-layer membrane patch of area  $40 r_c \times 40 r_c$  and width  $5.5 r_c$ .

apposing lipid mono-layers organized such that the hydrophilic lipid head groups are exposed to the solvent at both the membrane-solvent interfaces (see Figure 14). Using Dissipative Particle Dynamics (DPD) simulations, we investigate the interactions between synthetic amphiphilic protein channels and the bi-layer membrane. Each channel encompasses a tri-block architecture, with a hydrophobic stalk and two hydrophilic ends, both with and without end-tethers. Individual lipids are composed of a hydrophilic head group and two hydrophobic tails. Via this simulation approach, we begin with a stable lipid bi-layer membrane immersed in a hydrophilic solvent, and introduce the synthetic protein channel into the surrounding solution. The energetically unfavorable interaction between the solvent and the hydrophobic segment of the channel could potentially drive these synthetic channels to penetrate the membrane, with the hydrophobic stalk being buried within the hydrophobic domains of the bi-layer. We show that the insertion of a



synthetic channel into a membrane bi-layer is dependent upon the presence of end-tethers for perfect hydrophobic match between the channel and the membrane.

***Synthetic Protein Channel (No End-Tethers).*** The first model of a synthetic protein channel is comprised of a hydrophobic stalk with two hydrophilic ends. After we release the channel into the solvent medium, the channel diffuses in the solvent until it approaches the lipid bi-layer membrane surface. The lipid head groups are attracted to the hydrophilic ends of the channel but repel the hydrophobic shaft. Due to thermal fluctuations of the lipids and undulations of the membrane, segments of the lipid hydrophobic tails close to the lipid head group can be transiently exposed to the solvent. When the channel approaches a region of the bi-layer where the membrane hydrophobic region is temporarily exposed to the solvent, and the channel is oriented such that its hydrophobic stalk is near the exposed membrane hydrophobic region, the lipid tails wet the channel hydrophobic stalk (Fig. 14(a), (b)). As the increasing number of lipids wet the channel surface, the channel sinks into the hydrophobic region of the membrane, and thins the bi-layer below the channel (see Fig. 14(c)). The channel will tilt and sink simultaneously until one end of the channel reaches the membrane surface bound by the lower monolayer (see Fig. 14(d)). A pore is generated when the edge of the sinking channel end reaches the membrane-solvent interface on the opposite lipid mono-layer tears through membrane (see Fig. 14(f)). The lipids in the vicinity of the pore will reorganize such that their head groups will shield the membrane hydrophobic region at the pore edge from the solvent. The channel continues to reorient until one end of the channel has completely reached the membrane-solvent interface, and has assumed a trans-membrane configuration. Once the channel is inserted in a trans-membrane configuration, as shown in Fig. 14(e), it will remain mobile in the membrane but is unable to leave the membrane and dissolve in the solvent.

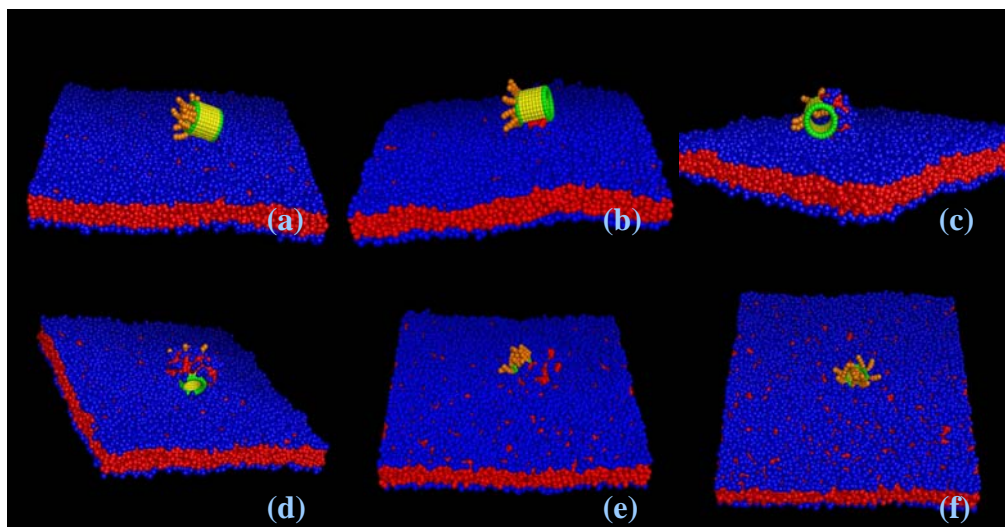


Figure 15. Insertion of a single end-tethered channel of radius  $1 r_c$  into a membrane.

***Single End-Tethered Synthetic Protein Channel.*** We repeated the numerical experiment using a single end-tethered synthetic protein channel. We place the single end-tethered synthetic protein channel in a solvent medium which also contains a tensionless fluid lipid bi-layer



membrane. The channel end-tethers are chains of hydrophilic beads which repel the membrane hydrophobic core but are attracted to the lipid head beads. The channel diffuses in the solvent until it approaches the membrane-solvent interface. The lipid head groups are attracted to both the tethered and non-tethered hydrophilic ends of the channel but repel the hydrophobic shaft. If the tethered end of the channel approaches the membrane-solvent interface, the tethers come into contact with the lipid head groups but do not allow the hydrophobic channel shaft to approach the membrane due to the chain conformational entropy and interaction energy penalty. However if the non-tethered end of the channel approaches the membrane, transient exposure of the lipid hydrophobic tails to hydrophobic shaft of the channel allows the lipids to wet the hydrophobic channel surface (see Figs. 15 (a), (b)). The single end-tethered channel follows an identical insertion mechanism as the channel without any end-tethers (see Figs. 15(c)-(f)).

**Double end-tethered synthetic protein channels:** We repeated the numerical experiment using a third model for the synthetic protein channels: a channel comprises of a hydrophobic stalk with hydrophilic ends and chains tethered to each end. The hydrophilic channel end-tethers are attracted to the lipid head groups but repel the membrane hydrophobic region. The tether conformational entropy and interaction energy penalty prevent the channel hydrophobic shaft from approaching the hydrophobic regions of the membrane. Therefore, the channel is unable to insert itself into the tensionless fluid membrane through absorption at the membrane-solvent interface.

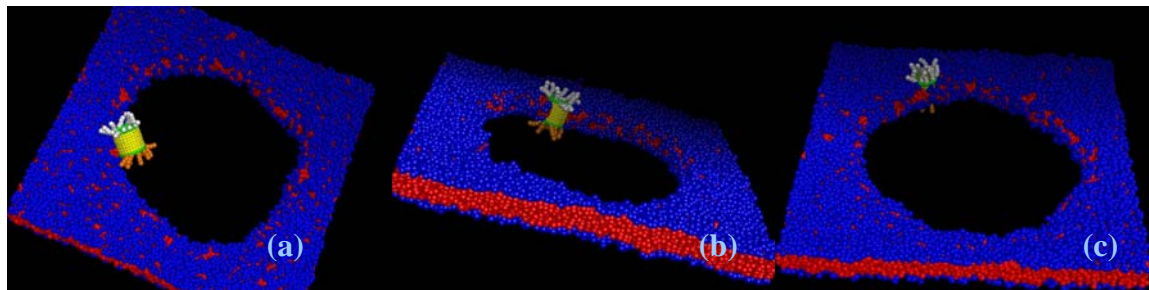


Figure 16. Insertion of a double end-tethered channel of radius  $1 r_c$  into a membrane through absorption at the pore edge.

We overcome the barriers imposed by the tethers at both ends by applying sufficient tension on the membrane so as to rupture the membrane and generate a stable pore, while preserving the original volume. We place the double end-tethered synthetic channel in a solvent medium containing a tensionless fluid lipid bi-layer membrane. When the membrane is stretched, the area per lipid increases simultaneously with an increase in the membrane tension, resulting in the thinning of the membrane. When the tension exceeds a critical threshold, regions of the membrane which have thinned sufficiently will perforate the membrane and form transient pores. One of the transient pores will become sufficiently long lived to allow the rearrangement of the lipid head groups around the pore edge to minimize exposure of the lipid hydrophobic tails to the hydrophilic solvent, and stabilize the pore. The pore will stabilize when the line tension balances the surface tension. The area per lipid is higher at the pore edge surface than at the bi-layer plane surface. In addition, the thermal fluctuations of the lipid head groups temporarily expose the lipid tail groups to the solvent. A combination of the higher area per lipid at the pore edge surface and the lipid head group thermal fluctuations imply that, on average, there is a larger exposure of the membrane hydrophobic region to the solvent at the pore edge surface than at the bi-layer plane. If the double end-tethered synthetic protein channel approaches the pore edge surface so that the

channel hydrophobic shaft is in close proximity with the hydrophobic region of the membrane which is exposed to the solvent, the channel will be attracted to the pore edge surface. Once the channel comes into contact with the membrane hydrophobic region at the pore edge, the neighboring lipids begin to wet the channel and gradually absorb the channel into the hydrophobic region such that the channel is oriented in a trans-membrane configuration with the hydrophilic end chains immersed in the solvent (see Fig. 16). Once the channel is completely absorbed into the membrane, it is mobile within the bi-layer. When the tension on the membrane is gradually reduced, the balance between the line and surface tensions decrease the pore size until the tension falls below the critical threshold. Below the critical threshold tension, the pore closes and the membrane returns to a tensionless fluid state with the synthetic channel inserted in a trans-membrane configuration.